

## Accepted Manuscript

Title: Multiphysics Model Investigating Performance of a Micromachined Floating Element Shear Stress Sensor

Authors: Nikolas Kastor, Zhengxin Zhao, Robert D. White

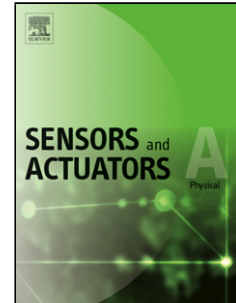
PII: S0924-4247(17)31193-7  
DOI: <https://doi.org/10.1016/j.sna.2017.11.004>  
Reference: SNA 10433

To appear in: *Sensors and Actuators A*

Received date: 11-7-2017  
Revised date: 24-10-2017  
Accepted date: 5-11-2017

Please cite this article as: Nikolas Kastor, Zhengxin Zhao, Robert D. White, Multiphysics Model Investigating Performance of a Micromachined Floating Element Shear Stress Sensor, *Sensors and Actuators: A Physical* <https://doi.org/10.1016/j.sna.2017.11.004>

This is a PDF file of an unedited manuscript that has been accepted for publication. As a service to our customers we are providing this early version of the manuscript. The manuscript will undergo copyediting, typesetting, and review of the resulting proof before it is published in its final form. Please note that during the production process errors may be discovered which could affect the content, and all legal disclaimers that apply to the journal pertain.



# Multiphysics Model Investigating Performance of a Micromachined Floating Element Shear Stress Sensor

Nikolas Kastor<sup>a</sup>, Zhengxin Zhao<sup>b</sup>, Robert D. White<sup>c</sup>

<sup>a</sup> PhD Candidate, Mechanical Engineering, Tufts University, 200 College Ave, Medford, MA 02155, USA

<sup>b</sup> Research Assistant, Mechanical Engineering, Tufts University, 200 College Ave, Medford, MA 02155, USA

<sup>c</sup> Associate Professor, Mechanical Engineering, Tufts University, 200 College Ave, Medford, MA 02155, USA, r.white@tufts.edu

## Highlights

- A multi-physics 3D model of a floating element shear stress sensor is developed.
- Complex forces interact with the sensor and contribute to total sensor output.
- Aerodynamic forces cause deflections in downstream, lift and pitch directions.
- Adding surface topology to the sensor increases pressure gradient sensitivity.
- Sensors must be designed with minimal topology to maximize shear sensitivity.

## Abstract

A MEMS floating element shear stress sensor has been developed for flow testing applications, targeted primarily at ground and flight testing of aerospace vehicles and components. A comprehensive numerical model of this sensor is described in this paper, quantifying the behavior of the mechanical components, fluid interaction, and electrostatics in three, non-coupled, 3-D numerical simulations: 1) A finite element model of the static element. 2) A steady state, incompressible, viscous, laminar, Newtonian computational fluid dynamics (CFD) model, for both flat and textured versions of the floating shuttle. 3) A finite element model of the capacitive sensing combs. The distribution of aerodynamic forces over the floating element was studied to determine which features contributed most to the total applied force and sensitivity. Shear stress forces account for 74% of the sensitivity of the flat sensor, with the remainder coming primarily from

pressure gradient effects. For a textured sensing element, while the total sensor sensitivity increases between 17% and 27%, only 34% of the output is due to shear forces, and the response is more nonlinear. Thus, a flat sensor with as little surface topology as possible is preferable to reduce pressure gradient sensitivity and nonlinearity, even though it may exhibit lower overall sensitivity to flow forces. In addition, the sensor is shown to not only deflect in the direction of flow due to shear forces, but also to lift away from the substrate and pitch its downstream edge away from the surface. Pitch rotation contributes as much as 37% of the output of the sensor for a textured element, but less than 1% for the flat element. For a perfectly symmetric device, differential measurement completely eliminates the contribution from lift. Overall, the model gives a more complete picture of the sensing mechanisms present in a floating element shear stress sensor, and demonstrates the aerodynamic complexities which motivate careful design and calibration of these types of sensors.

#### **Keywords**

Shear Sensor, Floating Element, Pressure Gradient, Modeling, FEA, CFD

## 1. Introduction

Wall shear stress and skin friction measurements are important in a variety of experimental fluid mechanics scenarios. These include such diverse applications as laboratory and field testing of space (during atmospheric flight), air, ground, and ocean-going vehicles, flow control and industrial flow applications in high shear stress environments such as injection molding or pipe flow, and in the flow of biofluids for circulatory system modeling or tissue engineering. The operating environments for wall shear stress sensing are many, and the levels of shear span multiple orders of magnitude. Steady and unsteady forces are of interest, as are feedback

applications for active flow control. In turbulent flow environments such as boundary layers on aircraft, the scales over which the shear stress changes may be small (sub millimeter scale) and fast (millisecond scale or faster) [1-5].

A number of established techniques for the measurement of wall shear stress exist, including oil film interferometry [6], boundary layer profile surveys, and thermal methods [1, 7-9]. Other authors have described optical force measurement methods using whispering gallery mode resonators [10, 11]. A recent paper introduces a method of using flow in an ionic fluid in communication with surface forces to measure stress [12]. These methods have various strengths and weaknesses. Sometimes, the measurements can be difficult to apply, or are indirect, relying on heat transfer analogies, or may not provide real time data [4, 5, 13-15]. MEMS floating element sensors are another option for sensing shear at the wall. These include capacitive [16-25] and piezoelectric [26] devices. MEMS floating element sensors can provide real-time, high bandwidth measurements, and have the potential for low topology, array sensing in multiple directions, and ease of use due to their direct electrical readout.

However, as with many of the other techniques, there are challenges associated with accurate calibration and application of MEMS floating elements. A primary concern is whether the floating element is truly measuring shear stress at the wall, or whether it might also be measuring stream-wise pressure gradients, acoustic pressures, or other features of the flow [25]. In order to understand these effects, MEMS floating element sensors have been typically modeled as a linear spring attached to a flat plate. The plate is assumed to experience uniform wall shear stress over its top surface, and the output  $Y$  is presumed to be proportional to the static lateral deflection of the element  $\delta$  as follows

$$Y = \Phi \delta = \Phi \frac{A}{k} \tau_w \quad (1)$$

where  $\Phi$  is the ~~electromechanical coupling~~ sensitivity coefficient, which depends on the transduction scheme (e.g. capacitive, piezoresistive, optical),  $k$  is the mechanical stiffness,  $\tau_w$  is the wall shear stress (usually this is assumed to be the wall shear stress present in the system before the element was introduced), and  $A$  is the physical surface area of the top of the sensor.

In this work, it is found that while linear spring mechanical models and linear transduction models are generally sufficient to describe the physics, restricting the model to one dimension is not sufficient. It appears that the interaction of the flow with the floating element is much more complex than is suggested by equation (1) because the element also experiences vertical motion and a pitching rotation. Therefore, we developed a more complete numerical model of a floating element shear stress sensor. The model includes three dimensional mechanical and electrostatic models, but focuses primarily on the complexities of the fluid flow around the three dimensional sensor topology. The major contributing aerodynamic forces are examined in an attempt to identify the source of the pressure gradient sensitivity observed in earlier experimental characterization [25]. To this end, two different sensor geometries are examined: one with a flat upper surface and a second with a textured surface composed of raised posts. It is shown that the addition of topology to the surface substantially increases pressure gradient sensitivity.

These results point to a need to design MEMS floating element sensors with few gaps and little surface topology in order to enhance the shear sensitivity while reducing pressure gradient sensitivity. In addition, it is shown that other aerodynamic forces, beyond simply surface shear on the top face and pressure gradient, produce measurable output. There is a net lift force and pitching moment, non-uniform shear over the top surface, pressures acting on lateral surfaces, and

recirculating flow below the element. The results provide guidance to researchers both in the design of MEMS floating element sensors and also in the method of calibration.

## 2. Sensor Design

The particular shear sensor that is modeled in this work has been described previously [25, 27-29]. The main feature of the structure is a floating element, shown in Figure 1, suspended above a small air gap by flexure beams. When traction is applied to the floating element, the element translates or rotates with, potentially, six degrees of freedom (presuming no internal deformation occurs). As the element moves it bends the flexures and changes the gap distance between the fingers in the electrostatic combs. Two sets of combs are provided so that a differential capacitance measurement can be performed. Ideally, the differential capacitance change would be linearly related to surface shear, and insensitive to other forces. To bring the element back to center when there is no applied load, the eight flexures provide a restoring force and moment. Raised posts 12 microns in height were added to the surface of the floating element to increase the drag on the upper surface. These features increase the total aerodynamic force on the element and thereby increase the sensor translation and output. An SEM image of the sensor, and the as-built geometric parameters measured from the SEM images, are given in Figure 2 and Table 1.

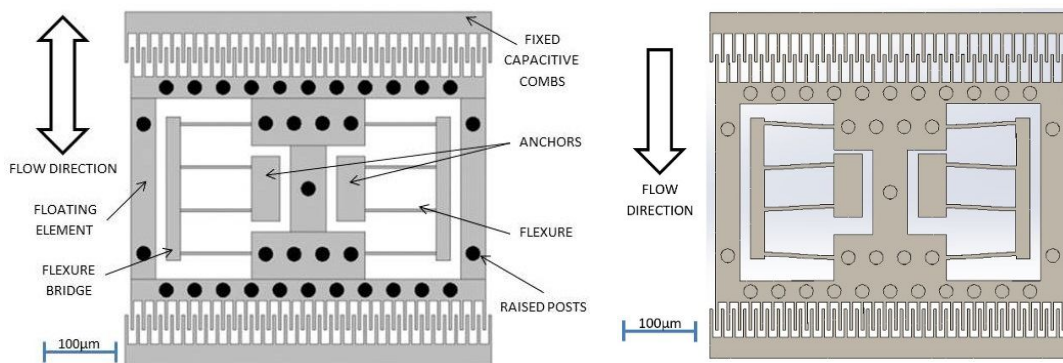


Figure 1: (Left) Schematic of the floating element shear stress sensor designed in [25, 27-29]. (Right) The sensing element after an applied load with the deformed shape exaggerated. The bottom combs are moved closer together as the top combs are pulled farther apart creating a differential capacitance proportional to the applied traction.

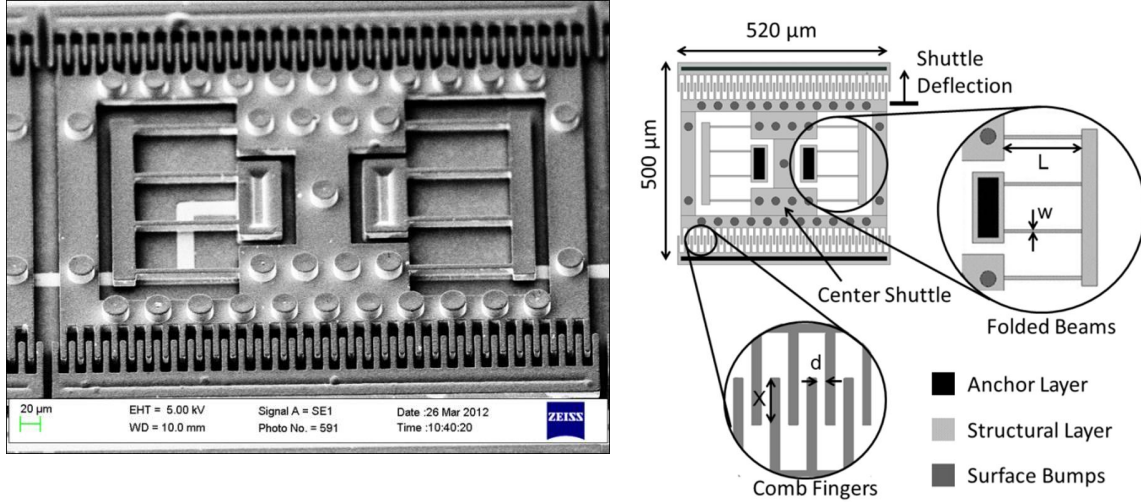


Figure 2: (Left) SEM image of a floating element shear stress sensor. (Right) Schematic showing geometric parameter labels as used in Table 1 [25, 27-29].

Geometric Parameter and Symbol	Value
Finger gap, $d$	2.88 μm
Finger width	5.13 μm
Finger overlap, $X$	20 μm
Number of comb fingers, $N$	64
Thickness of structure, $t$	8.8 μm
Width of folded beam, $w$	5.13 μm
Length of folded beam, $L$	99.2 μm
Height of bump	11.7 μm
Diameter of bump	24.7 μm
Height of air gap below shuttle	5.2 μm
Shuttle top area, $A_m$	0.085 mm <sup>2</sup>

Table 1: Structure geometry as manufactured, measured from SEM images.

The model developed here is broken into three parts: (1) Determination of forces applied by the flowing fluid, (2) the deflection of the sensing element as a result of those fluid forces, and (3) the result of that deflection on the comb capacitance. Due to the very small motions of the

element compared to the size of the gaps, the three models can be treated as uncoupled. This will be verified when model results are examined below. The overall model structure is diagrammed in Figure 3.

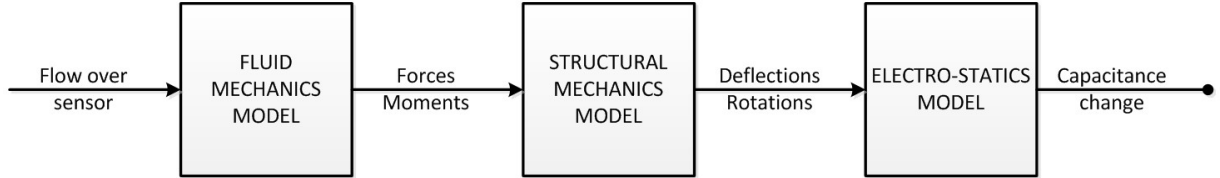


Figure 3: System model block diagram.

A steady, laminar, incompressible, 3D computational fluid dynamics (CFD) simulation was used to describe the fluid flow around the sensor geometry and determine the aerodynamic forces. 3D linear elastic finite element analysis (FEA) was used to determine structural stiffness. Finally, a 3D electrostatic finite element model was used to extract the change in capacitance due to structural motion. The combination of the results of these three models can be expressed as a linear (small deflection) model analytically as

$$\Delta C = \Phi_y \frac{1}{k_y} \underbrace{\left( A\tau_w + V \frac{\partial P}{\partial y} \right)}_{F_D}_{\delta_y} + \Phi_z \underbrace{\frac{F_L}{k_z}}_{\delta_z} + \Phi_\theta \underbrace{\frac{M_\theta}{k_\theta}}_{\delta_\theta} \quad (2)$$

where the differential capacitance change  $\Delta C$  is produced by flow-direction motion  $\delta_y$ , out-of-plane motion  $\delta_z$ , and pitch angle  $\delta_\theta$  with respective sensitivities  $\Phi_y$ ,  $\Phi_z$ , and  $\Phi_\theta$ . The element motion is driven in the flow-direction by the total drag force  $F_D$ , which is decomposed into a wall shear component  $A\tau_w$  and a pressure gradient component  $V \frac{\partial P}{\partial y}$ .  $A$  is the effective top surface area

of the element, which in previous work was shown experimentally to be similar to the physical top surface area [25].  $V$  is the effective volume of the element. If the flow field were maximally simplified, so that pressure varies along the sensor only in the  $y$ -direction, the integration of pressure force over the surfaces of a rectangular prism of dimensions  $L_x \times L_y \times L_z$  results in a pressure difference  $\frac{\partial P}{\partial y} L_y$  multiplied by the end area  $L_x \times L_z$  for a net force of  $\frac{\partial P}{\partial y} L_x L_y L_z$ , that is,  $V \frac{\partial P}{\partial y}$ . However, as demonstrated experimentally in [25] and explored computationally in this work, the effective volume may be considerably greater than the physical volume, due to the more complex flow fields present in the actual geometry.

The motion is also affected by the net lift force  $F_L$ , and the net pitching moment  $M_\theta$ .  $k_y$ ,  $k_z$  and  $k_\theta$  are the mechanical element stiffnesses to flow-direction motion, lift motion and pitch rotation, respectively. The other three rigid body degrees of freedom (cross-stream displacement, yaw, and roll rotations) are neglected due to the ability of the differential capacitance sense scheme to reject the following: 1) Common-mode motions, 2) symmetry of the flow in the test scenario, which will impose no net force or moment to excite those three degrees of freedom, and 3) higher (5 to 70 times) mechanical stiffness for these three directions.

### 3. Structural Mechanics

First, a 3D structural mechanics model was produced using Finite Element Analysis (FEA) to create a relationship between applied load and deflection. The goal is to extract the 6 mechanical stiffnesses; one for each rigid body degree-of-freedom (DOF) for the floating element. Since the goal of the model is to determine the ultimate capacitive sensitivity to motion, the motion of the

element (displacement and angular rotation) is measured from the finite element model at the location of the base of the finger combs by area averaging over the face.

In order to facilitate modeling, the geometry of the shear sensor was simplified. As seen in Figure 4, the capacitive combs and posts were removed because they do not contribute to the stiffness of the structure. Circular fillets with radii taken from the SEM images of the as-built element were included at each of the joints. The definition, the axis directions, and the rotations are shown in Figure 4. Intended operation of the sensor will have the primary direction of fluid flow aligned with the Y-axis.

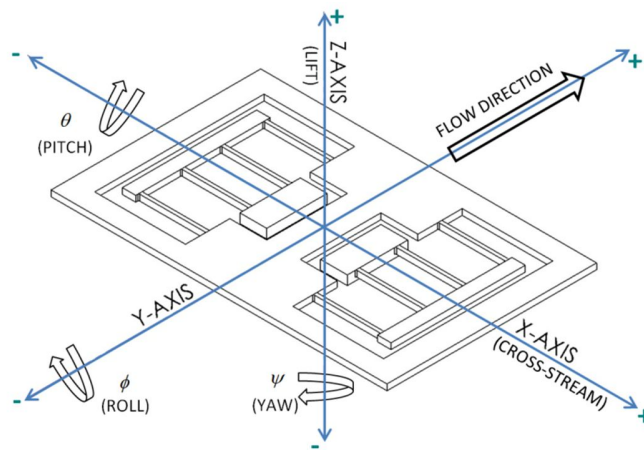


Figure 4: Global coordinate system. The Y-axis is in line with the fluid flow direction, the X-axis is transverse (cross-stream) to the direction of flow and the Z-axis is the out-of-plane (lift) direction. Rotation about the X-axis (Pitch), Y-axis (Roll) and Z-axis (Yaw) are denoted by  $\Theta$ ,  $\phi$ , and  $\psi$ , respectively.

Fixed boundary conditions were imposed on all 6 nodal degrees of freedom on the surface at the base of the anchors. A distributed load was applied over the top and bottom surface of the element in either the vertical or horizontal direction to produce motion. The distributed load was made to vary linearly across the element surface in order to produce a net moment. In all cases the load was designed such that the net force and moment for all 5 degrees of freedom not under examination was zero.

The simulation was performed in COMSOL Multiphysics using a small deformation, linear elastic model. The Young's modulus of the electroplated nickel was taken to be  $E=205 \text{ GPa}$  as measured by Luo et al. for a similar electroplating process for MEMS structures [30]. The Poisson's ratio was taken to be the bulk value for nickel  $0.31$  [31]. Although, Namazu et al. indicate that plated nickel films may have a Poisson's ratio as low as  $0.24$  [32], reducing the Poisson's ratio to  $0.24$  increases the rotational stiffness by approximately  $2\%$ , and has less than  $0.5\%$  effect on the translational spring constants.

The mesh used tetrahedral elements with quadratic shape functions. At least 3 elements were used across the thickness of narrow regions in the model, and mesh refinement about all of the small features (such as internal corners) was employed. A displacement based formulation was used. A convergence study was run by reducing the number of elements across thin regions to 2. This resulted in a  $1\%$  increase in stiffness; thus the solution was considered converged. The default direct MUMPS solver with pivoting was used.

The results of the structural mechanics simulation are arranged in Table 2 with an example deformation plot in Figure 5. Note that the deformation plot is exaggerated by a factor of more than  $10,000$ . From the results we see that the sensor is significantly more compliant for  $y$  (flow),  $z$  (lift) direction translations, and pitching rotation about the  $x$ -axis ( $k_\theta$ ) than for the other degrees-of-freedom. This is desirable, as the sensor is intended to measure primarily flow-direction forces. The higher compliance for pitch, lift, and flow-direction deflections also partially motivates the model reduction from 6 degrees of freedom to 3 degrees of freedom, as previously described in equation (2).

Stiffness Coefficient	Value	Unit
Cross-stream, $k_x$	21200	N/m
Flow-Direction, $k_y$	440	
Lift direction, $k_z$	636	
Pitch, $k_\theta$	$2.13 \cdot 10^{-6}$	N·m/rad
Roll, $k_\phi$	$1.25 \cdot 10^{-5}$	
Yaw, $k_\psi$	$1.47 \cdot 10^{-5}$	

Table 2: The six linear spring coefficients, one for each degree of freedom of the sensor structure, as extracted from the 3D FEA structural simulation.

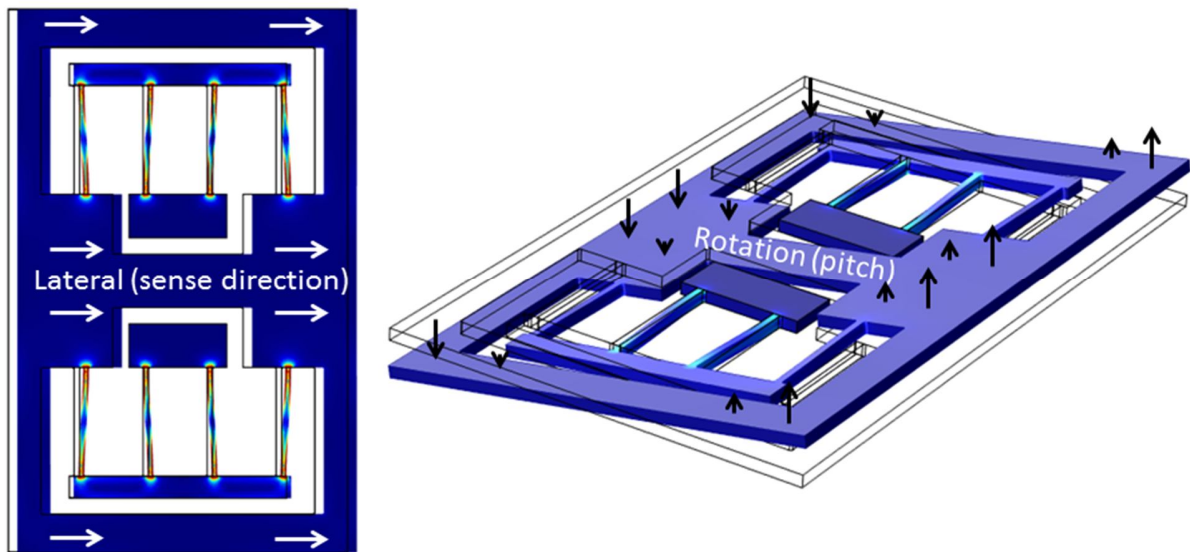


Figure 5: Two example results of the FEA structural simulation showing the lateral (downstream direction) deformation and the rotation (pitch) deformation.

#### 4. Fluid Mechanics

A computational fluid dynamics (CFD) model was used to determine the total aerodynamic loading on the floating element, as well as to investigate the distribution of loads over the surface, and the types of flow patterns present. The model is a three dimensional, steady state, incompressible, viscous, laminar flow model presuming a Newtonian fluid. Models, both with

and without the raised posts, were considered and the effect of the posts on the aerodynamic loading is quantified in this paper.

The physical sensor was tested in a laminar flow cell, as described in [29] and [25]. This flow cell produces Poiseuille slot flow in a slot 28 mm wide and of varying heights of 0.300 mm, 0.400 mm and 0.530 mm. The narrow slot height was intended to create high shear forces at the wall while maintaining laminar flow conditions. Flow experiments were run at a series of volume flow rates from 0 to 40 standard cubic feet per hour (SCFH). These flow rates result in area average fluid velocities between 0 and 37.5 m/s. For a direct comparison to experiment, a rectangular computational fluid domain was used, as shown in Figure 6. The system experiences fully developed laminar slot flow, therefore the inlet boundary condition of the model was defined as a Poiseuille parabolic velocity profile in the vertical direction with zero velocity variation in the cross-stream direction. The outlet was a zero pressure boundary condition. The entire height of the flow cell was modeled, so the top boundary condition was a rigid, no slip wall. The sensor itself was also considered as a rigid, no slip boundary condition. It should be noted that the motion of the sensor in response to aerodynamic forces is very small, less than 1% of the smallest gap, thus justifying the rigid boundary condition. Symmetry boundary conditions were used on either side of the control volume because the element and element-array geometry is symmetric. Although it is difficult to see in Figure 6, the small gap under the floating element and the gaps between the comb fingers are part of the fluid domain. The air density is taken to be  $1.21 \text{ kg/m}^3$  and the kinematic viscosity is taken to be  $2 \cdot 10^{-5} \text{ Pa}\cdot\text{s}$ .

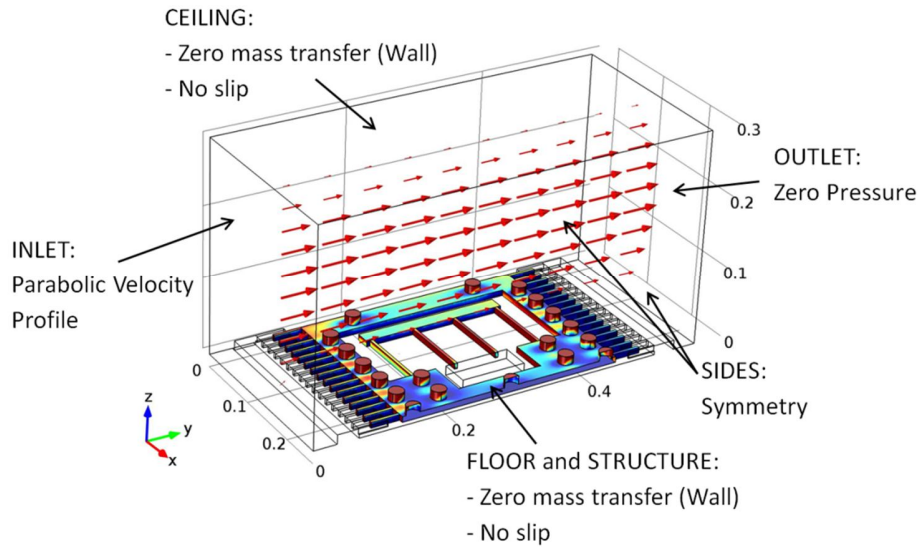


*Figure 6: The full CFD geometry including the sensing element and control volume. Dimensions in mm. Boundary conditions are indicated. This particular image shows the sensor with the raised posts, but both cases with and without posts were considered. The red arrows indicate the fluid velocity. The dominant Poiseuille profile is evident. The pseudocolor shading on the surface of the element indicates shear stress magnitude. The height of the channel was varied in imitation of experimental conditions. This particular case has a 0.3 mm high channel.*

The resulting surface stresses (shear and pressure) from the CFD model were integrated across all surfaces of the element, including comb fingers and flexures, to determine total flow-direction force, lift force, and the pitching moment about the center of mass. Cross-stream force, yaw moment, and roll moment are identically zero due to the symmetry of the flow and element geometry. To span the experimental cases (0 to 40 SCFH) described in [25], solutions were gathered for seven channel heights between  $H=0.3$  mm and 0.53 mm, and for a series of different area average flow rates between 0 and 56 m/s.

The results for total aerodynamic forces on the element are shown in Figure 7. Similar to a Moody diagram, the total force is plotted against Reynold's number based on slot height of the flow cell and the area average inlet velocity. Different curves are given for different values of relative roughness, where relative roughness in this case is defined as the total thickness of the structure  $h$  divided by the slot height  $H$ . The structure thickness is 25  $\mu\text{m}$  for the sensor with raised

posts and 14  $\mu\text{m}$  for the sensor without raised posts. It should also be noted that in the highest flow rate case, the Reynold's number is less than 1400 and the Mach number is less than 0.2, justifying the laminar, incompressible flow assumptions.

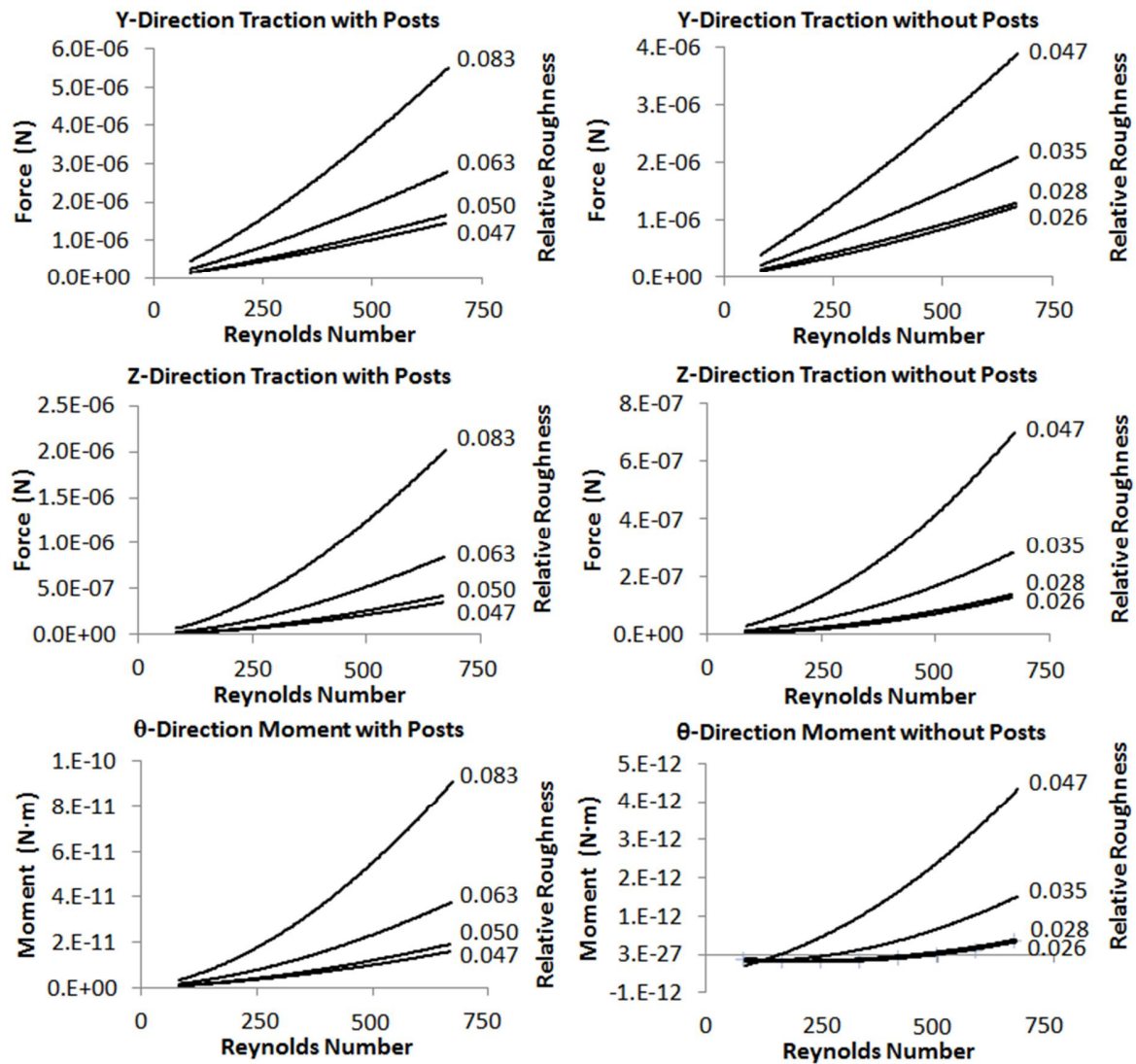


Figure 7: CFD results showing traction on the sensor with and without posts in the flow (Y), lift (Z) and pitch ( $\theta$ ) directions as a function of Reynolds number (based on the slot height of the flow cell and the area average flow velocity), and the relative roughness ( $h/H$ ), defined as the topology of the flow sensor ( $h$ ) divided by the duct height of the flow cell ( $H$ ).

A few important conclusions can be drawn from these results. First, it is seen that aerodynamic forces on a floating element are more complex than simply shear acting over the top face. In addition to flow-direction forces, the sensor experiences a net lift and net pitching moment. The forces and moment for the highest flow case, when combined with the results of the mechanics model, indicate that the structure will experience at most 13 nm of downstream (flow-direction) deflection, 3 nm of vertical (lift) deflection, and 0.003 degrees of pitching rotation. The pitching is downstream edge up, which results in 15 nm of edge displacement away from the substrate at the downstream edge. In all cases this causes less than a 1% change in the smallest gap, justifying the use of a rigid boundary condition for the element. However, the lift motion and displacement due to rotation are of a similar order of magnitude as the flow-direction motion, and so can be expected to contribute measurably to sensitivity.

Second, it is seen that adding posts to the surface of the sensor increases the net flow-direction force by nearly a factor of 1.5. Posts have an even greater effect on pitching moment and lift, increasing the moment by a factor of 20 and lift by a factor of 2.5. This will result in a larger output signal in terms of capacitance change. However, the stresses on the posts have components in the shear and normal directions increasing sensitivity to pressure gradient effects.

Finally, we see that aerodynamic forces are influenced not only by the Reynold's number of the flow, but also the relative roughness of the flow (with the sensor topology treated as a wall roughness), at least in this thin slot-flow calibration. This is true for relative roughness values greater than approximately 3% or 5% for the sensor without and with posts respectively, suggesting that the added surface roughness will impact the measurement results. Precisely what the magnitude of this impact is will depend on the type of flow. Therefore, to achieve the best

calibration results, the slot height should be more than 20 times greater than the maximum sensor topology.

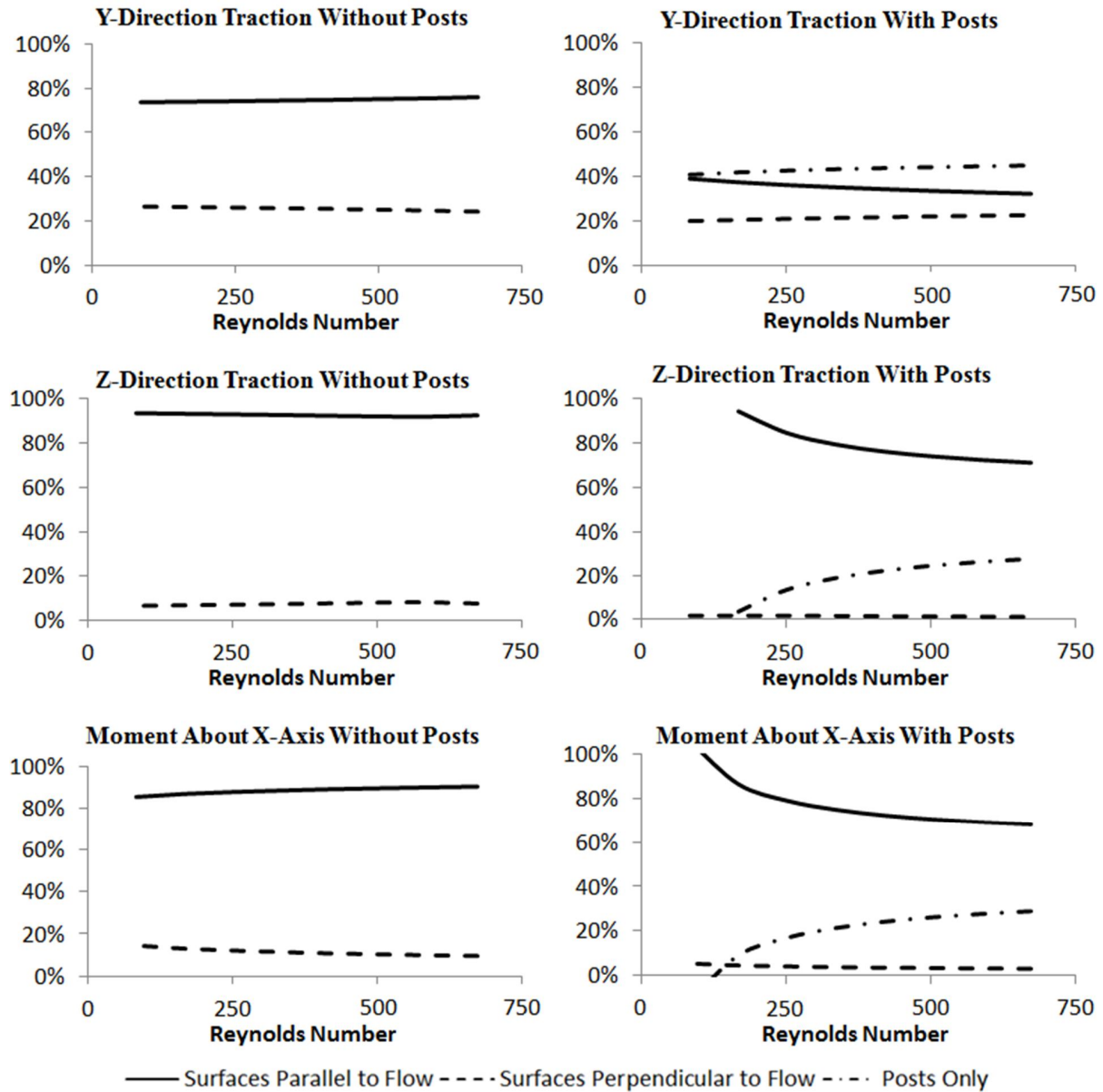


Figure 8: CFD results showing the fractional contributions (vertical-axis) from different surfaces to the total flow direction (Y-direction) and lift direction (Z-direction) forces, as well as pitching moment (rotation about X-axis), on the sensor element. Results are given for one choice of duct height ( $H=300\ \mu\text{m}$ ) which is a relative roughness of 0.083 with posts and 0.043 without posts. Results are plotted against Reynolds number (horizontal-axis) computed based on the area average inlet flow velocity and the hydraulic diameter slot height.

Figure 8 shows how the forces are distributed on different surfaces of the element. The fractional contribution of total force provided by surfaces parallel to the flow direction, surfaces perpendicular to the flow direction, and the post structures are plotted. The lift force (z-direction) comes primarily from surfaces parallel to the flow due to a pressure difference between the gap below the element and the free stream. For the y-direction (flow-direction) traction case with no posts, nearly 30% of the force comes from surfaces perpendicular to the flow, consequently significant pressure gradient sensitivity is expected. With the addition of posts to the structure, 40% of the total traction on the element is dominated by the interaction of the flow with the posts. This is the source of the increased total force observed. It is important to understand that this force is not simply a shear effect. It is a combination of shear and pressure gradient effects as the flow interacts with the topology of the surface.

In addition, it can be seen that for the structures with no posts, the contributions are roughly constant with Reynold's number. Conversely, the forces introduced by the posts vary substantially with Reynold's number in a nonlinear fashion. This suggests that the sensor with raised topology will show a more complex, nonlinear response to changing flow speed, and therefore, will have an output that is more difficult to interpret.

## 5. Electrostatics

The remaining part of the model is the electrostatics component, which will predict the change in capacitance due to structural deformation by solving the differential form of Gauss' law for static electric fields in a finite element framework. The electrical output measured by the sensor is the change in capacitance. In the model, one conductor is held at zero potential, and the second conductor at a potential of 1 V. The resulting dot product of electric displacement  $\vec{D}$  and electric

field  $\vec{E}$  was integrated over the three dimensional volume between and around the conductors to determine the total change in stored electrostatic energy,

$$\Delta E = \int_{\Omega} (\vec{D} \cdot \vec{E}) dV \quad (3)$$

The capacitance is then computed from the relationship between energy and voltage

$$C = 2 \frac{\Delta E}{V^2} \quad (4)$$

The conductor boundaries were then moved by known increments to model lateral, vertical, and pitching displacements of the sensor, and the capacitance recomputed. This method yields a three-dimensional result for the capacitance change due to different structural displacements, including all three dimensional effects. Both the air dielectric above and around the structure, as well as the glass substrate under the structure, are modeled. The relative permittivity of air is taken to be  $\epsilon_r=1$ , and that of glass to be  $\epsilon_r=4.2$  [33]. The glass permittivity was verified experimentally by measuring the capacitance of a metal structure on the same type of soda lime glass and back calculating the relative permittivity via FEA simulation. It was determined that the value was  $4 \pm 0.4$  and thus the uncertainty in simulating capacitance is expected to be 1.73%. This includes the uncertainty in  $\epsilon_r$  as well as the results of a study of the numerical sensitivity of capacitance to changes in the glass dielectric constant.

A quarter element 3D model, shown in Figure 9, was used with symmetry boundary conditions on the mirror planes. The top half of the model is the surrounding air and the bottom half is the glass substrate. The glass substrate is 0.5 mm thick as manufactured, but only 0.100 mm was used since the field does not penetrate deep into the glass. For the same reason, only

0.100 mm of the air height above the combs was used. Sensitivity studies were conducted to ensure that this truncation of the domain had less than a 1% influence on computed capacitance.

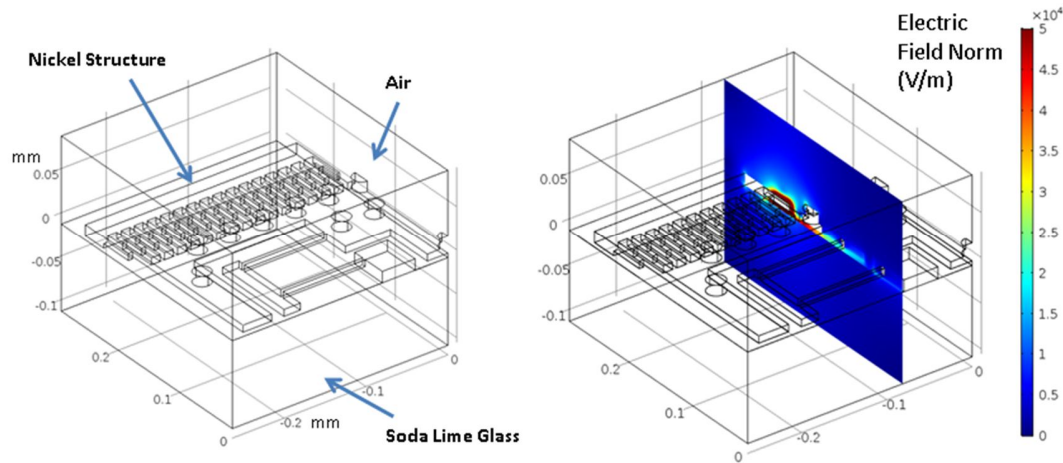


*Figure 9: (Left) Entire geometry including the sensing element, glass substrate and surrounding air control volume. Units are in mm. (Right) Results for electric field (V/m). The field is concentrated in the region of small gaps near the combs.*

Three scenarios were solved to provide the required relationship between deflection and capacitance change: the structure was deflected in the flow (Y) direction, in the out-of-plane (Z) direction, and pitched about the central axis. A large deflection model was run first to observe the nonlinear shape of the curve and then a higher resolution study was conducted near the operating point (zero deflection point) to extract the local linear sensitivity. For the small deflection study, the magnitudes of the deflections were selected to be approximately three times the maximum deformations predicted by fluidic and structural analysis for the highest flow scenario.

A convergence study was conducted with 13 runs in which the resolution of the narrow gaps was varied from 4 to 16 elements. The total capacitance converged to within 0.02% error with a resolution of 9 or more elements across the gap. The change in capacitance between the maximum and minimum deflection converged to better than 4% at 4 elements across the gap, and

did not improve with further mesh refinement. All results are reported for a mesh with 10 elements across the narrow gaps.

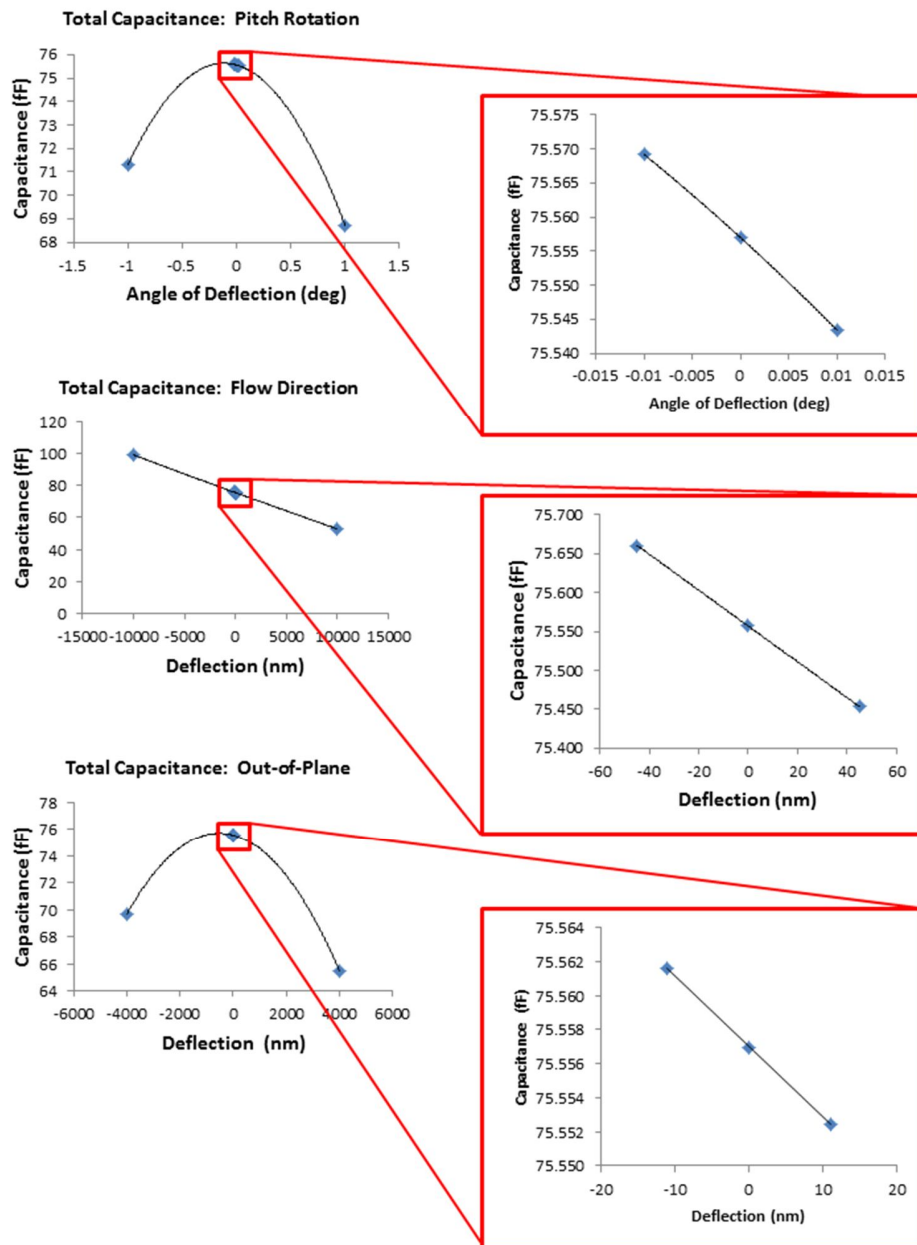


Figure 10: Converged results for the capacitance change as a function of three rigid body deflections (flow direction, vertical direction, and pitching rotation). The results are reported for a single set of combs along one side of the element.

Figure 10 shows the results of the electrostatic model. As seen in Figure 1, the sensing element has two sets of combs that measure capacitance (one up-stream and one down-stream). The results are presented as computed capacitance for only one of those two sets of combs. The static capacitance for one set of combs on one element is 75.6 fF. For the entire 128 element chip we would expect to see 9.68 pF of capacitance per side. These large deflection studies show the expected nonlinearities experienced when the deflected distance becomes a significant fraction of the structural gap distance. It is particularly important to note that the pitching and vertical deflection results show an approximately linear response near zero, not a parabolic response as might be expected if the structure were considered without including the symmetry-breaking effects of the substrate. In the refined small range studies, the predicted electrostatic sensitivity is linear to better than  $R^2 > 0.99$  over a range that extends to three times the normal operating deflection of the sensor.

The total differential capacitance measured by the system is the result of the net effect of the two sides of the capacitive element. For flow-direction motion, the effect will double (one set of combs engages, one disengages). For vertical motion, the effect will exactly cancel (assuming identical combs on either side of the device). For pitching motion, the effect will again double (one set of combs pitches up, one pitches down). Note again the importance of the asymmetry in the pitching capacitance curves. If the glass substrate did not generate asymmetry, and the curves were parabolic centered at zero, then both pitching and vertical motion would cancel as common mode effects. However, with the asymmetry, pitching contributes a net differential capacitance change.

Un-deflected Capacitance	75.6 fF	151 fF
Electrostatic Coefficient	Single Sided	Differential
Lateral (positive deflection downstream)	2.3 aF/nm	$\Phi_y = 4.6$ aF/nm
Vertical (positive deflection away from the substrate)	-0.41 aF/nm	$\Phi_z = 0$
Pitching (positive edge down towards substrate)	1.3 fF/deg	$\Phi_\theta = -2.6$ fF/deg

Table 3: Linear fit ( $R^2 > 0.99$ ) for the electrostatic response to structural deflection. Results are given for a single set of combs along one edge, and also a differential result for the downstream edge capacitance change minus the upstream edge capacitance change. Note that the vertical deflection is a common mode signal and so creates no differential output. However, the pitching motion is antisymmetric and so generates a differential output, as does the lateral deflection. The differential results are the electromechanical coupling coefficients from equation (2),  $\Phi_y$ ,  $\Phi_z$ , and  $\Phi_\theta$ . Also note that in operation, 128 elements act in parallel on the chip, increasing the sensitivity for the entire device by a factor of 128.

Figure 11 shows these capacitance contributions and motions. Differential capacitance change is considered to be the capacitance of the downstream capacitor minus the capacitance of the upstream capacitor. The net result is an *increase* of 4.6 aF/nm differential capacitance change due to flow-direction motion, and a net *reduction* of 2.6 fF/deg differential capacitance change due to shuttle pitch rotation. The shuttle rotation, as predicted by the fluid mechanics simulation, is upstream edge down towards the substrate and downstream edge up away from the substrate. This results in a reduction of the downstream capacitance and an increase in the upstream capacitance, thus reducing the overall differential capacitance sensed by the device. The lift effect cancels in the differential result, but for each side the capacitance decreases by 0.41 aF/nm for the predicted lifting motion (away from substrate).

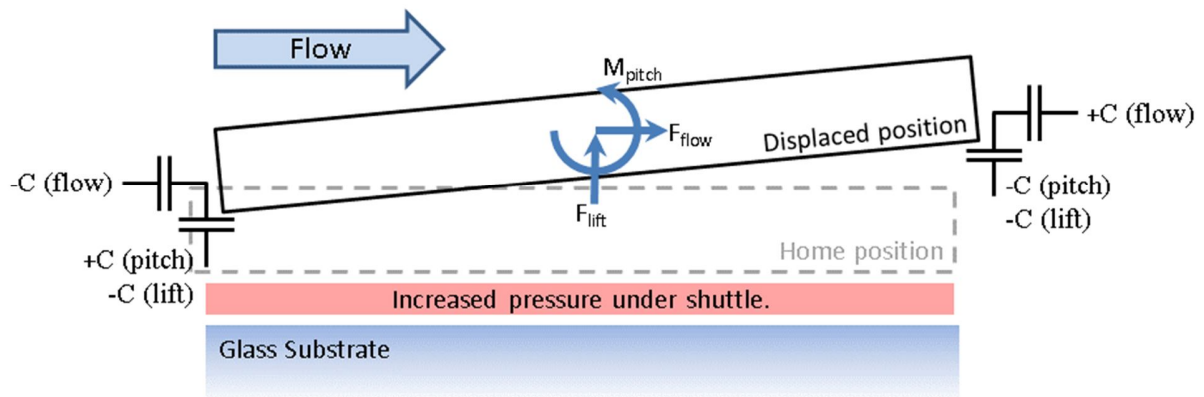


Figure 11: Schematic showing motion of the element. The element moves downstream, increasing the differential capacitance. It lifts away from the substrate, with no net effect on differential capacitance. Finally it pitches downstream edge away from the substrate, reducing the differential capacitance.

The surface charge density on the interface between the glass substrate and the air volume is assumed to be zero in the model, although this surface does have the possibility of holding a charge. In practice, we do not know the magnitude of surface charge on the glass, and it is possible that surface charging at this interface could be a source of drift in measurements. In addition, there is the possibility that surface charge could be influenced by atmospheric conditions such as humidity. To investigate this, electrostatic models were run with  $3 \cdot 10^{-6} \text{ C/m}^2$  and  $3 \cdot 10^{-5} \text{ C/m}^2$  charge density at the free glass surface. These densities were selected based on the results in [34], where glass beads were subjected to air flow and the surface charge measured. The highest charge measured was  $3 \cdot 10^{-6} \text{ C/m}^2$ . Hence, we consider  $3 \cdot 10^{-5} \text{ C/m}^2$  to be a worst case scenario, although we do not have direct measurements of glass surface charging for our flow case. The computational results shown in Figure 12 indicate that the single-sided capacitive sensitivity may change by as much as 60% for the highest surface charge case. However, the differential sensing mechanism mitigates much of this. For the worst case charging scenario, the change in differential sensitivity is less than 10%.

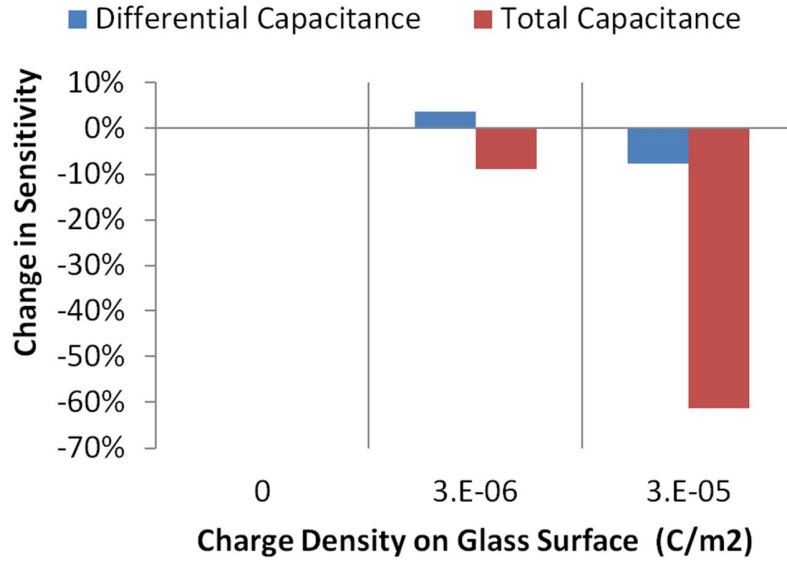


Figure 12: The effect of surface charge on the glass substrate was investigated by varying the charge density at the surface from 0 to  $3 \times 10^{-5}$  C/m<sup>2</sup> [34] on the surface of the glass substrate below the sensing element. Changing the charge density dramatically changes the total capacitance of one comb. However, differential capacitance exhibits less than 10% change in sensitivity for the highest charge density.

## 6. Combined Response

With all three parts of the model complete, the full system response to flow can be determined, using the global sensor model of equation (2),

$$\Delta C = \Phi_y \frac{1}{k_y} \underbrace{\left( A\tau_w + V_{eff} \frac{\partial P}{\partial y} \right)}_{F_D} + \Phi_z \frac{F_L}{\underbrace{k_z}_{\delta_z}} + \Phi_\theta \frac{M_\theta}{\underbrace{k_\theta}_{\delta_\theta}} \quad (5)$$

For model validation, the results are compared quantitatively with experimental data from [25]. The result shown in Figure 13 is for the case of 300  $\mu$ m duct height and the geometry with raised posts. Wall shear in the horizontal axis of Figure 13 is determined from pressure gradient measurements which, for laminar slot flows, are directly related to wall shear by:

$$\tau_w = -\frac{1}{2}h \frac{\partial P}{\partial x} \quad (6)$$

The wall shear determined by this method was in close agreement to that expected for laminar slot flow based on measured volume flow rate [25].

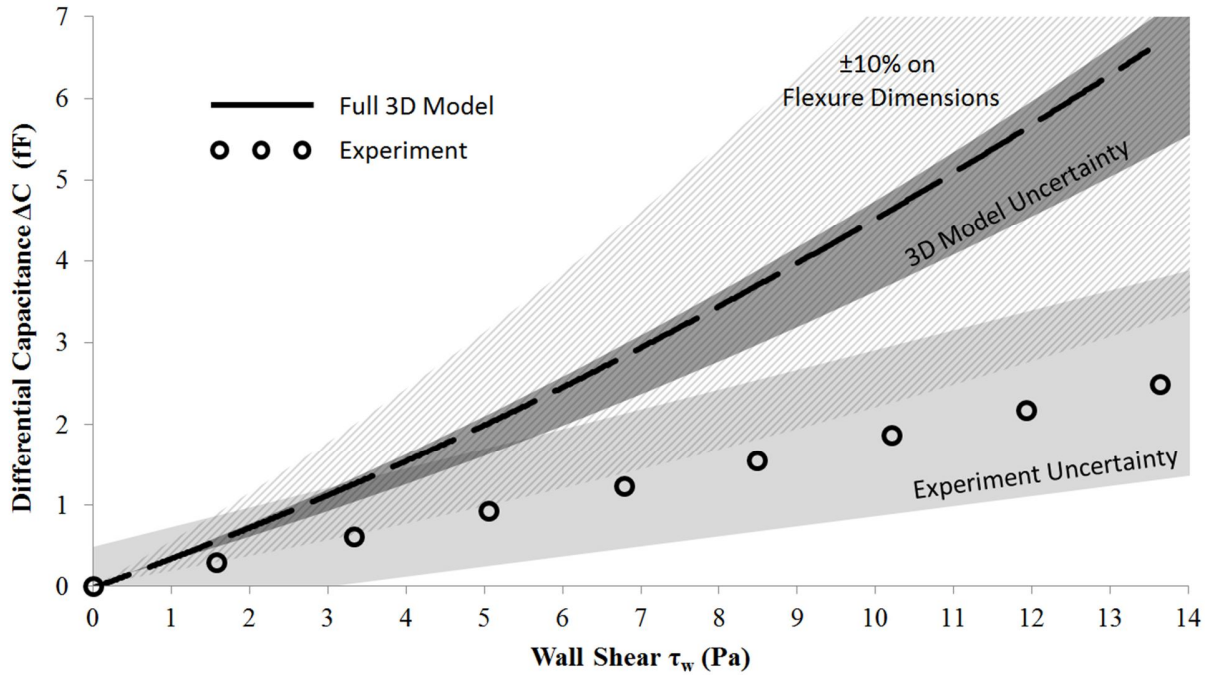


Figure 13: Results of the coupled model for the case of a sensor with posts in the 0.3 mm height duct. Sensor output for the entire chip (128 elements acting in parallel) is shown as a function of wall shear. The model is compared to experimental data measured by our group [25]. Uncertainty regions on the model include: (1) an inner region that accounts for uncertainty in surface charge, dielectric constant, convergence, corner fillets and gap height (2) an outer region that additionally accounts for +/-10% uncertainty in structure thickness and width. Uncertainty on the experiment includes duct height machining tolerance, duct surface roughness uncertainty, flow rate measurement uncertainty, capacitance measurement uncertainty, and uncertainty on the density and viscosity of the flowing air.

The total predicted differential capacitance output for the entire chip, which has 128 elements acting in parallel, is plotted as a function of wall shear in the flow cell. Uncertainty estimates on the experiment include the capacitance readout electronics, manufacturing accuracy on the flow cell height and roughness, the uncertainty on the measured volume flow rate of the

flow, and the uncertainty of the properties of the flowing air. Uncertainty estimates on the computed result include the estimated convergence error, effects of potential variation in glass dielectric constant, sensitivity to possible unknown charge density on the glass substrate, and uncertainty on the fillet radius at structure corners. This is the inner uncertainty region in the plot of model predictions, and is estimated at +6%/-20%.

A second larger uncertainty region on the model estimates uncertainty due to variation in structural dimensions. Since the structure is primarily in bending, and bending stiffness is proportional to the 4<sup>th</sup> power of cross-sectional dimension (cross-sectional area moment of inertia varies as the 4<sup>th</sup> power of linear dimension), a +/-10% change in linear dimension results in a +46%/-34% change in bending stiffness. Since capacitance varies inversely with stiffness, this results in a -32%/+52% change in capacitance. The measured dimensions used for beam width and thickness (5.1  $\mu\text{m}$  and 8.8  $\mu\text{m}$ , respectively) were taken from a similar device fabricated in the same process. However process variation from run to run and across the wafer could easily produce 10% variation in beam cross-sectional dimensions. Knowing this, the measured and modeled response agree within experimental uncertainty.

The beam cross-sectional dimension is the most significant source of uncertainty in the model, and is consistent with our experience in modeling MEMS sensors in general. There is enough uncertainty from geometry, material properties, and boundary conditions that exact quantitative matches can be challenging to achieve. However, trends are often well captured, and so models are very useful for predicting how an output will change given a change in an input parameter, or, as is our aim here, are useful for exploring the relative contributions of various effects to the total output.

Figure 14 shows the results from four cases – with and without posts, and in high and low flow scenarios ( $Re=500$  and  $Re=1400$ ). From this figure we can draw the following general conclusions. For a structure without posts (low surface topology), 74% of the output signal comes from flow-direction deflection due to shear stresses acting on the element, 26% of the output comes from differential pressure forces acting on the element, and a negligible fraction of the output comes from pitching. Although net lift is experienced by the element, for a perfectly symmetrical device no net differential capacitance is contributed by lift. This is true at both high and low flow rates, with only 0.5% change. For the structure with posts (high surface topology), the total output increases by between 17% (at low flow) and 27% (at high flow) over the element with no surface structures.

This increased sensitivity due to high surface topology might appear to be advantageous, but it comes at a cost. The element with surface structures achieves only 34% of its total positive output (flow-direction motion) from shear stresses. 22 % comes from pressure gradient forces and 44% come from fluidic interaction directly with the posts. Pitching is due to a combination of pressure and shear forces acting both on the body of the element and the post structures and reduces sensitivity by 7% (at low flow) and by 37% (at high flow). Although adding surface posts increases the total output from the element, the structure is no longer primarily a shear stress sensor, but is sensing a combination of flow features, and also exhibits a more nonlinear response to the flow due to flow rate dependent pitching.

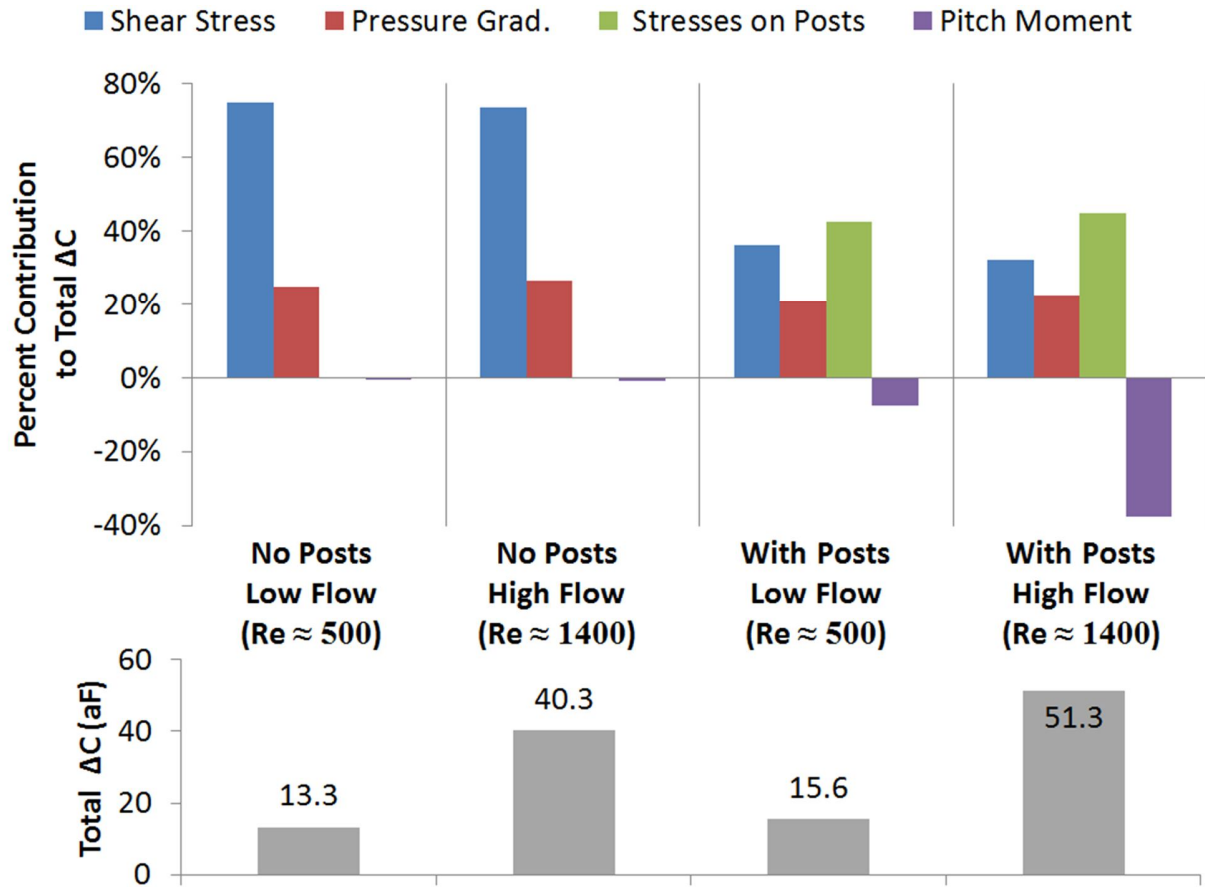


Figure 14: (Top) The fractional contribution to the total differential capacitance output for low flow and high flow cases for sensors with and without posts. The contributions from lateral forces (shear stress) normal forces (pressure gradient) forces on the posts, and pitching moment are given. (Bottom) The total differential capacitance output (in aF) for the entire 128 element chip in each of the 4 cases.

## 7. Conclusions

A complete numerical model of a floating element shear stress sensor, including three-dimensional mechanical, fluid and electrostatic components was developed. The model was used to investigate complexities of the aerodynamic forces interacting with the sensor, and determine their contributions to the total sensor output. Results were compared back to experimental

measurements from [25] for validation. Two models were considered to investigate the effects of surface topology on the sensor: one with structured posts and one with a flat top surface.

From this model, it was determined that in addition to the desired shear stress interaction with the sensor, there are lift forces and pitching moments, non-uniform shear over the top surface, pressures acting on all surfaces and recirculating stagnant flow under the element. The net aerodynamic forces cause the sensor to deflect downstream, as expected, but also to lift away from the substrate and to pitch the downstream edge away from the substrate. Lift displacements are significant, at 1/8 to 1/4 of the flow-direction displacements. Pitching displacements are much greater for the element with posts (8.6 arcseconds) compared to the element without posts (0.4 arcseconds). Pitching contributes as much as 37% of the total output for the sensor with posts, but makes very little contribution to the output for the sensor without posts. Lift contributes no net differential output for the ideal symmetric device.

Adding surface topology (e.g. raised posts) to the top of the sensing element increases the net flow force and total sensitivity to flow, but achieves this by increasing sensitivity to pressure gradient effects and pitching, rather than shear stress, and increasing nonlinearity. The aerodynamic forces are influenced by the Reynold's number for the slot flow considered in this work, as well as the roughness of the wall including the sensor topology. This interaction contributes to nonlinear variation in forces with increasing Reynold's number, particularly for the sensor with surface posts, suggesting that sensors should be designed with as little surface topology as possible if shear stress is the quantity to be sensed. Future sensor designs should minimize gaps and surface topology to maximize shear sensitivity while minimizing pressure gradient sensitivity and nonlinearity.

Pressure gradient sensitivity appears to be important for sensors of this type in slot flows with high pressure gradients such as those used for calibration, and so must be accounted for experimentally when calibrating devices of this type. This work demonstrates that aerodynamic interactions with the sensor element can be complex; therefore, further study is needed to extend this investigation of sensor performance to other flow scenarios such as turbulent boundary layers, turbulent pipe flow, wakes, and separated flows of various kinds.

## References

- [1] L. Löfdahl, V. Chernoray, S. Haasl, G. Stemme, and M. Sen, "Characteristics of a hot-wire microsensor for time-dependent wall shear stress measurements," *Experiments in Fluids*, vol. 35, pp. 240-251, 2003.
- [2] L. Löfdahl and M. Gad-el-Hak, "MEMS applications in turbulence and flow control," *Progress in Aerospace Sciences*, vol. 35, pp. 101-203, 1999.
- [3] L. Löfdahl and M. Gad-el-Hak, "MEMS-based pressure and shear stress sensors for turbulent flows," *Measurement Science and Technology*, vol. 10, p. 665, 1999.
- [4] J. W. Naughton and M. Sheplak, "Modern developments in shear-stress measurement," *Progress in Aerospace Sciences*, vol. 38, pp. 515-570, 2002.
- [5] M. Sheplak, L. Cattafesta, T. Nishida, and C. B. McGinley, "MEMS shear stress sensors: promise and progress," in *24th AIAA aerodynamic measurement technology testing conference. Florida Univ Gainesville mechanical and aerospace engineering*, 2004.
- [6] L. Tanner and L. Blows, "A study of the motion of oil films on surfaces in air flow, with application to the measurement of skin friction," *Journal of Physics E: Scientific Instruments*, vol. 9, p. 194, 1976.
- [7] Y. Hasegawa, C. Okihara, T. Yamada, K. Komatsubara, K. Iwano, Y. Sakai, *et al.*, "Smooth-surfaced flexible wall shear stress sensor fabricated by film transfer technology," *Sensors and Actuators A: Physical*, vol. 265, pp. 86-93, 2017.
- [8] E. Kälvesten, C. Vieider, L. Löfdahl, and G. Stemme, "An integrated pressure—flow sensor for correlation measurements in turbulent gas flows," *Sensors and Actuators A: Physical*, vol. 52, pp. 51-58, 1996.
- [9] B. Van Oudheusden, "Silicon thermal flow sensors," *Sensors and Actuators A: Physical*, vol. 30, pp. 5-26, 1992.
- [10] U. Ayaz, T. Ioppolo, and M. Ötügen, "Wall shear stress sensor based on the optical resonances of dielectric microspheres," *Measurement science and technology*, vol. 22, p. 075203, 2011.

- [11] U. Ayaz, T. Ioppolo, and M. Ötügen, "Direct measurement of wall shear stress in a reattaching flow with a photonic sensor," *Measurement Science and Technology*, vol. 24, p. 124001, 2013.
- [12] C. Hughes, D. Dutta, Y. Bashirzadeh, K. Ahmed, and S. Qian, "Measuring shear stress with A Micro Fluidic sensor to improve aerodynamic efficiency," in *53rd AIAA Aerospace Sciences Meeting. AIAA*, 2015.
- [13] H. Fernholz, G. Janke, M. Schober, P. Wagner, and D. Warnack, "New developments and applications of skin-friction measuring techniques," *Measurement Science and Technology*, vol. 7, p. 1396, 1996.
- [14] K. Winter, "An outline of the techniques available for the measurement of skin friction in turbulent boundary layers," *Progress in aerospace sciences*, vol. 18, pp. 1-57, 1979.
- [15] C.-M. Ho and Y.-C. Tai, "Micro-electro-mechanical-systems (MEMS) and fluid flows," *Annual Review of Fluid Mechanics*, vol. 30, pp. 579-612, 1998.
- [16] M. A. Schmidt, R. T. Howe, S. D. Senturia, and J. H. Haritonidis, "Design and calibration of a microfabricated floating-element shear-stress sensor," *IEEE Transactions on Electron Devices*, vol. 35, pp. 750-757, 1988.
- [17] A. Padmanabhan, "Silicon micromachined sensors and sensor arrays for shear-stress measurements in aerodynamic flows," Aerospace Computational Design Laboratory, Dept. of Aeronautics & Astronautics, Massachusetts Institute of Technology 1997.
- [18] A. Padmanabhan, M. Sheplak, K. Breuer, and M. Schmidt, "Micromachined sensors for static and dynamic shear-stress measurements in aerodynamic flows," in *Solid State Sensors and Actuators, 1997. TRANSDUCERS'97 Chicago., 1997 International Conference on*, 1997, pp. 137-140.
- [19] A. Padmanabhan, H. Goldberg, K. D. Breuer, and M. A. Schmidt, "A wafer-bonded floating-element shear stress microsensor with optical position sensing by photodiodes," *Journal of microelectromechanical systems*, vol. 5, pp. 307-315, 1996.
- [20] T. Pan, D. Hyman, M. Mehregany, E. Reshotko, and S. Garverick, "Microfabricated shear stress sensors, part 1: design and fabrication," *AIAA journal*, vol. 37, pp. 66-72, 1999.
- [21] J. Zhe, V. Modi, and K. R. Farmer, "A microfabricated wall shear-stress sensor with capacitive sensing," *Journal of microelectromechanical systems*, vol. 14, pp. 167-175, 2005.
- [22] V. Chandrasekharan, J. Sells, J. Meloy, D. P. Arnold, and M. Sheplak, "A microscale differential capacitive direct wall-shear-stress sensor," *Journal of microelectromechanical systems*, vol. 20, pp. 622-635, 2011.
- [23] A. A. Barlian, S.-J. Park, V. Mukundan, and B. L. Pruitt, "Design and characterization of microfabricated piezoresistive floating element-based shear stress sensors," *Sensors and Actuators A: Physical*, vol. 134, pp. 77-87, 2007.

- [24] J. Shajii, K.-Y. Ng, and M. A. Schmidt, "A microfabricated floating-element shear stress sensor using wafer-bonding technology," *Journal of Microelectromechanical Systems*, vol. 1, pp. 89-94, 1992.
- [25] Z. Zhao, M. Shin, J. M. Gallman, and R. D. White, "A microfabricated shear sensor array on a chip with pressure gradient calibration," *Sensors and Actuators A: Physical*, vol. 205, pp. 133-142, 2014.
- [26] R. P. Williams, D. Kim, D. P. Gawalt, and N. A. Hall, "Surface micromachined differential piezoelectric shear-stress sensors," *Journal of Micromechanics and Microengineering*, vol. 27, p. 015011, 2016.
- [27] Z. Zhao, "MEMS floating element sensor array for wall shear stress measurement under a turbulent boundary layer," 2014.
- [28] Z. Zhao, K. R. Long, J. Gallman, and R. D. White, "Flow Testing of a MEMS Floating Element Shear Stress Sensor," in *52nd American Institute of Aeronautics and Astronautics Aerospace Sciences Meeting*, 2014.
- [29] Z. Zhao, M. Shin, R. D. White, and J. Gallman, "A MEMS floating element with bump shear stress sensor array on a chip," in *the Proceedings of the 51st AIAA Aerospace Sciences Meeting, Grapevine, TX*, 2013, pp. 2013-0626.
- [30] J. Luo, A. Flewitt, S. Spearing, N. Fleck, and W. Milne, "Young's modulus of electroplated Ni thin film for MEMS applications," *Materials Letters*, vol. 58, pp. 2306-2309, 2004.
- [31] M. Baucchio, *ASM Metals Reference Book* vol. 3rd: ASM International, 1993.
- [32] T. Namazu and S. Inoue, "Characterization of single crystal silicon and electroplated nickel films by uniaxial tensile test with in situ X-ray diffraction measurement," *Fatigue & Fracture of Engineering Materials & Structures*, vol. 30, pp. 13-20, 2007.
- [33] P. R. H. Gray, P.J.; Lewis, S.H.; Meyer, R.G., *Analysis and Design of Analog Integrated Circuits*: John Wiley & Sons, 2009.
- [34] S. Nieh and T. Nguyen, "Effects of humidity, conveying velocity, and particle size on electrostatic charges of glass beads in a gaseous suspension flow," *Journal of Electrostatics*, vol. 21, pp. 99-114, 1988.



**Nikolas Kastor** received his B.S. degree in mechanical engineering from Fairfield University in 2008 where he graduated magna cum laude receiving mathematics, research and engineering honors. He received his M.S. degree part-time from Tufts University in 2014 while working in industry. From 2008 to 2014, Nikolas worked as a project engineer and design engineer in the fields of transducers and consumer products research and development generating many products and patents. Nikolas is currently a PhD candidate and NSF IGERT Soft-Material Robotics Fellow at Tufts University. He has served as a teaching assistant for various mechanical engineering and design courses; and received the mechanical engineering teaching assistant award in the spring of 2015. His research interests include, but are not limited to, MEMS sensing and actuation as well as soft robotics where he has authored several publications. Nikolas has presented work at multiple technical conferences and demonstrated his research in North America, Europe and Asia. He is a member of ASME, IEEE and RAS.



**Zhengxin Zhao** received M.S in 2010 and Ph.D in 2014, both from Tufts University, Medford, MA, for working on MEMS floating element shear stress sensor. After graduation, he joined MEMSIC Inc, Andover, MA as a MEMS design engineer, and has designed and developed new MEMS flow sensors and modules. In 2016, he took on the role as a product engineer at Analog Devices Inc., Wilmington, MA and is responsible for new product development of inertial MEMS sensors.



**Robert D. White** received B.S. and M.S. degrees in mechanical engineering from the Massachusetts Institute of Technology in 1999, and the Ph.D. degree in mechanical engineering from the University of Michigan, Ann Arbor, in 2005.

He worked as a MEMS Test Engineer at the C.S. Draper Laboratories, Cambridge, MA on MEMS gyroscopes and accelerometers from 1999-2000. In 2005, he joined Tufts University, Medford, MA as an Assistant Professor of mechanical engineering. In 2011 he was promoted to Associate Professor. In 2013, Prof. White benefited from a 6 month sabbatical leave at the NASA Ames Research Center working in the Experimental Aerophysics branch working on wind tunnel instrumentation. His primary research interest is in the design, fabrication, modeling, and testing of microsystems, particular acoustic devices and aerodynamic measurement technologies, with additional work in inner ear mechanics, acoustics and vibrations, and mechatronics. He teaches in the areas of microsystems, acoustics, dynamics, and controls. Since 2007, he has directed the Tufts Micro and Nano Fabrication Facility. He is the author of multiple technical publications and patents.

Prof. White received a C.S. Draper Fellowship in 1998, the NSF Graduate Research Fellowship in 2001, a Rackham Predoctoral Fellowship in 2004, and the Tufts Outstanding Contributor to Graduate Education in 2011, and the Faculty Teaching and Mentoring Award from the Engineering Graduate School in 2017. He is a member of the ASA, ASME, and AIAA.